Journal of Materials Chemistry A

ROYAL SOCIETY OF CHEMISTRY

PAPER

View Article Online
View Journal | View Issue

Cite this: J. Mater. Chem. A, 2024, 12, 8724

Synergistic electronic structure modulation of Pt using V_2O_3 and V_8C_7 for enhanced deuterium evolution performance†

Yanfeng Li,‡ Yuan Sheng,‡ Liangbin Shao, Yuanan Li, Weiwei Xu, Shijie Zhang, Fangjun Shao* and Jianguo Wang *

Received 8th January 2024
Accepted 1st March 2024

DOI: 10.1039/d4ta00150h

rsc.li/materials-a

The slower kinetics of the deuterium evolution reaction (DER) than the hydrogen evolution reaction (HER) renders conventional Pt-based HER catalysts inefficient in the DER. Their further improvement requires precise tuning of intermediate adsorption energy which is already near optimum on pure Pt. Herein, we achieved superior DER/HER performance by combining Pt and a dual support system consisting of V_2O_3 and V_8C_7 that exert different electronic effects on Pt. In 1 M NaOD (NaOH) and 0.5 M D_2SO_4 (H_2SO_4), the optimal Pt/V_2O_3/V_8C_7 catalyst exhibited low overpotentials of 37 mV (15 mV) and 49 mV (45 mV) at a current density of 10 mA cm^{-2}, respectively. Its mass activity based on the amount of Pt was up to 9 times higher than that of commercial Pt/C, leading to a reduction of cell voltage by 0.5 V in PEM electrolysis of D_2O at 1000 mA cm^{-2}. X-ray photoelectron spectroscopy and underpotential H deposition showed that electron-withdrawing effects of V_2O_3 over-weakened intermediate adsorption on Pt/V_2O_3 while Pt/V_8C_7 had insufficient metal–support interaction of such kind. A balanced effect was only achieved with the dual support system, which accounts for the excellent performance of Pt/V_2O_3/V_8C_7. This study provides a new perspective on the modulation of metal–support interaction in Pt-based electrocatalysts and demonstrates potential application of the Pt/V_2O_3/V_8C_7 in industrial production of D_2.

1. Introduction

In comparison to hydrogen (H_2) which finds widespread applications in energy and chemical production,[1–3] deuterium (D_2) holds unique promise in isotope studies, nuclear magnetic resonance experiments, and deuterated medicines.[4–8] Traditional methods for D_2 production, such as liquid hydrogen distillation, metal hydride technology, and gas chromatography, entail complexities.[9,10] Electrolysis of heavy water (D_2O) for D_2 production emerges as a simple and green alternative.[11,12] While alkaline electrolysis is the dominant technique for H_2 production due to its cost-effectiveness, it faces challenges such as impurity issues and slow response rates.[13–16] In contrast, the proton exchange membrane (PEM) electrolysis technology produces high-purity H_2 directly and tolerates frequent load changes, despite a higher capital and maintenance cost.[17–20] The high purity standards and value of D_2 and its downstream products thus make PEM electrolysis of D_2O more promising.

There is limited research on deuterium gas production, with the primary focus being on hydrogen–deuterium separation.[21–24] For example, Xu *et al.* developed a Pt/NGF catalyst with a separation factor of 6.83 for hydrogen and deuterium.[23] Zeng *et al.* conducted a systematic study on the separation performance of hydrogen and deuterium using a PEM device.[24] These studies mainly revolve around the development of efficient HER catalysts, achieving hydrogen–deuterium separation through the enrichment of deuterium water. Recently, Zheng *et al.* employed machine learning and density functional theory (DFT) methods to screen potential HER/DER catalysts.[25] Wang *et al.* also investigated the HER/DER kinetics on the Pt (111) surface using DFT.[26] Thus, experimental development of efficient catalysts for the DER remains urgently needed.

The lower zero-point energy of D-containing species compared with their H-containing counterparts leads to an elevated activation barrier and slower rates in the DER than in the HER.[27–30] For example, Pt is well known for its fast HER kinetics which is limited by the desorption of the H intermediate.[31–33] The effect is exacerbated in the DER due to the stronger adsorption of D, making state-of-the-art Pt/C HER catalysts struggle to achieve optimal performance in the DER. Further optimization of the kinetics requires careful tuning of the intermediate adsorption energy, as it is already close to ideal on neat Pt. Alloying Pt with another metal has been a widely

Institute of Industrial Catalysis, College of Chemical Engineering, State Key Laboratory Breeding Base of Green-Chemical Synthesis Technology, Zhejiang University of Technology, Hangzhou 310032, China. E-mail: shaofj@zjut.edu.cn; jgw@zjut.edu.cn

† Electronic supplementary information (ESI) available. See DOI: https://doi.org/10.1039/d4ta00150h

‡ Y. F. Li and Y. Sheng contributed to this work equally.

adopted strategy which also offers the benefit of reduced noble metal loading.[34–36] However, the harsh operating conditions in PEM electrolysis accelerate the degradation of Pt alloy catalysts by surface reconstruction and leaching of the non-noble component.[37–40] Introducing strong metal–support interaction has been proven effective, but such a method is less flexible as the change in intermediate adsorption energy is material-specific which cannot be tuned easily.[41–44] The overall performance of the catalyst is further complicated by the corrosion-resistance and electrical conductivity of the support material.[45–47]

Recently, transition metal carbides have been found to be a class of durable catalyst support materials with good electrical conductivity.[47–50] For example, vanadium carbide MXenes showed favorable metal–support interaction with Pt to decrease the adsorption strength of H and enhance its HER activity.[51] Unfortunately, their practicality is limited by the cumbersome and hazardous synthesis. Vanadium carbide (V_8C_7) is easier to synthesize while also possessing high corrosion resistance and excellent conductivity, making it an ideal carbide support.[52–54] However, Pt/V_8C_7 exhibits suboptimal hydrogen adsorption, requiring further tuning. We have shown previously the potential of V_2O_3 to adjust the electronic structure and hydrogen adsorption energy of the supported metal catalyst, which is envisaged to also apply to Pt-based catalysts.[12] It is hypothesized that a V_2O_3/V_8C_7 dual support system can combine the advantages of both components and offer more precise tuning of metal–support interaction due to the additional degree of freedom introduced.

This study presents the development of a $Pt/V_2O_3/V_8C_7$ catalyst by exploiting the synergy between the V_2O_3 and V_8C_7 support materials, demonstrating superior DER/HER performance in both acidic and alkaline solutions compared to similarly prepared Pt/V_2O_3 and Pt/V_8C_7 as well as commercial Pt/C. We further show the practical potential of the catalyst in a PEM electrolyzer for D_2 and H_2 production from D_2O and H_2O, where $Pt/V_2O_3/V_8C_7$ displayed up to 20% reduction in cell voltage compared with commercial Pt/C at current densities of 1000–2000 mA cm^{-2} and excellent stability. The origin of its remarkable performance is explored by extensive materials characterization and electrochemical analysis including H and Cu underpotential deposition experiments in particular.

2. Results and discussion

2.1 Catalyst morphology and structure

The method of catalyst synthesis is summarized in Fig. 1a. The samples are named according to their main composition which is determined by the amount of glucose and NH_4VO_3 used. The support materials are denoted by V_2O_3, V_2O_3/V_8C_7, and V_8C_7 as the amount of glucose increases, while GC denotes the support material obtained without NH_4VO_3, *i.e.*, glucose-derived carbon. The corresponding Pt-loaded catalysts are referred to as Pt/V_2O_3, $Pt/V_2O_3/V_8C_7$, Pt/V_8C_7, and Pt/GC, respectively. The scanning electron microscopy (SEM) image in Fig. 1b shows the V_2O_3/V_8C_7 support material to consist of nanoparticles ~50 nm in size. Reducing the amount of glucose used in the hydrothermal synthesis caused an apparent increase in particle size of the support material, while increasing the amount of glucose had minimal effect (Fig. S1†).

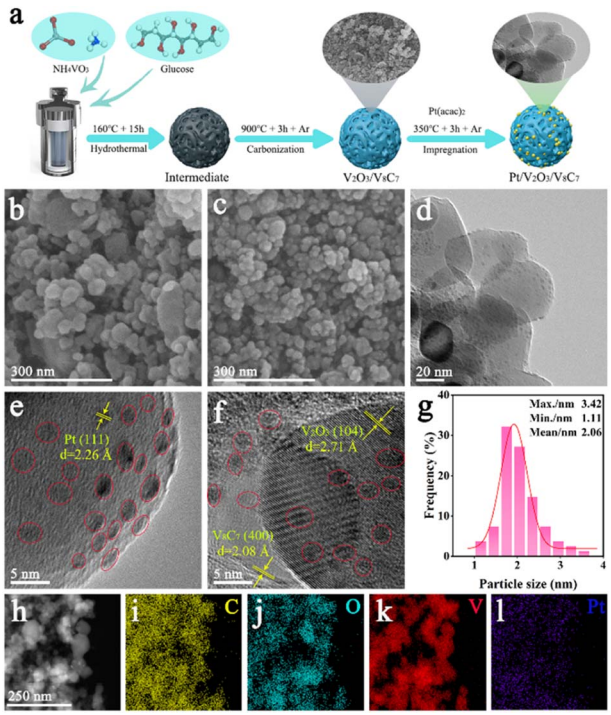

Fig. 1 Synthesis and morphology of $Pt/V_2O_3/V_8C_7$. (a) Schematic diagram of the synthesis procedure, (b) SEM image of V_2O_3/V_8C_7, (c) SEM image and (d–f) TEM images of $Pt/V_2O_3/V_8C_7$, (g) corresponding size statistics of Pt particles, and (h–l) elemental mapping of C, O, V and Pt in $Pt/V_2O_3/V_8C_7$.

After Pt was loaded, the overall morphology did not change noticeably as seen in Fig. 1c and S2.† The transmission electron microscopy (TEM) images of $Pt/V_2O_3/V_8C_7$ in Fig. 1d–f confirm the SEM findings, revealing the support material to be aggregations of crystalline nanoparticles. Pt can be found in the form of nanoclusters evenly distributed on the surface of V_2O_3/V_8C_7. The Pt nanoclusters exhibit a unimodal size distribution centered around 2 nm (Fig. 1g). The lattice fringes observed in Fig. 1e have a spacing of 2.26 Å, corresponding to the (111) plane of face-centered cubic Pt.[55–57] Fig. 1f shows lattice fringes extending throughout the individual particles of the support material, indicating them to be single crystals. The lattice spacing of 2.08 Å observed in Fig. 1f is assigned to the (400) planes of cubic V_8C_7, while the lattice spacing of 2.71 Å belongs to the (104) planes of hexagonal V_2O_3.[55,58–61] Elemental mapping results in Fig. 1h–j show slight segregation of C and O in the catalyst which is consistent with the TEM observation of V_8C_7 and V_2O_3 single crystals. On the other hand, V and Pt exhibit uniform distribution as indicated by Fig. 1k and l. In the absence of V_8C_7 and V_2O_3, however, the glucose-derived carbon formed 500 nm spheres on which Pt was poorly dispersed and grew to 10–20 nm particles (Fig. S3).

Through N_2 adsorption–desorption analysis, the physical surface area and pore structure of the different support materials were investigated. All the adsorption–desorption isotherms

Table 1 Textural properties of catalyst supports

Sample name	S_{BET} (m^2 g^{-1})	V_{micro} (cm^3 g^{-1})	V_{meso} (cm^3 g^{-1})
V_2O_3	105	0.03	0.10
V_2O_3/V_8C_7	242	0.07	0.35
V_8C_7	644	0.23	0.30
GC	473	0.16	0.23

presented in Fig. S4† show mixed Type I and Type IV characteristics according to the IUPAC classification, indicating the coexistence of micropores and mesopores. As seen in Table 1, the specific surface area calculated of the carbide or oxide support by the Brunauer–Emmett–Teller method (S_{BET}) increases with the amount of glucose used during synthesis, and the micropore volume (V_{micro}) showed a similar trend. In view of the single crystal nature of the V_2O_3 and V_8C_7 particles and their 50 nm size, the micropores are unlikely to be associated with these phases but should be attributed to carbonaceous structures derived from excess glucose dehydration products. These structures are probably responsible for the increase in mesopore volume as well. On the other hand, the surface area and pore volume of GC are lower than those of V_8C_7, which can be attributed primarily to structural variances in the carbon materials. It is speculated that during the carbonization process, V species migrate from their original position to coagulate into crystallites and leave behind voids. Additional pores can be generated by the release of gas from the oxidation of carbon by the V oxides.

The crystal structures of Pt/V_2O_3, Pt/V_8C_7, and $Pt/V_2O_3/V_8C_7$ catalysts were characterized using X-ray diffraction (XRD). In the XRD patterns presented in Fig. 2a, Pt/V_2O_3 displays well-resolved diffraction peaks consistent with hexagonal V_2O_3 (PDF#34-0187), while those of Pt/V_8C_7 correspond to cubic V_8C_7 (PDF#35-0786).[55,62–65] The diffraction pattern of $Pt/V_2O_3/V_8C_7$ shows characteristic peaks of both phases, indicating its support material to be a mixture of hexagonal V_2O_3 and cubic V_8C_7. It is noteworthy that the signal intensity of the V_8C_7 phase is stronger than that of the V_2O_3 phase in $Pt/V_2O_3/V_8C_7$, suggesting that the former dominates in the composition of the catalyst. Although all three catalysts exhibit sharp and distinct diffraction peaks, no signal from Pt was clearly detected due to the small size of Pt nanoclusters and the low loading of Pt that result in relatively weak X-ray scattering. In contrast, as shown in Fig. S5,† Pt diffraction peaks are observable in the XRD pattern of Pt/GC. The particle size of Pt NPs on Pt/GC was calculated to be around 10–20 nm by the Scherrer equation.[46,66] It confirms the relatively poor Pt dispersion in Pt/GC found in Fig. S3.†

Fig. 2b shows the X-ray photoelectron spectroscopy (XPS) survey spectra of the catalysts. Major core level peaks of C, O, V, and Pt can be clearly observed. The relative intensity of the O 1s and V 2p peaks compared with that of C 1s exhibits a clear decreasing trend from Pt/V_2O_3 to $Pt/V_2O_3/V_8C_7$ and then Pt/V_8C_7. This corroborates the findings made through N_2 adsorption–desorption experiments and points to increasing coverage of the carbonaceous material as the amount of glucose used

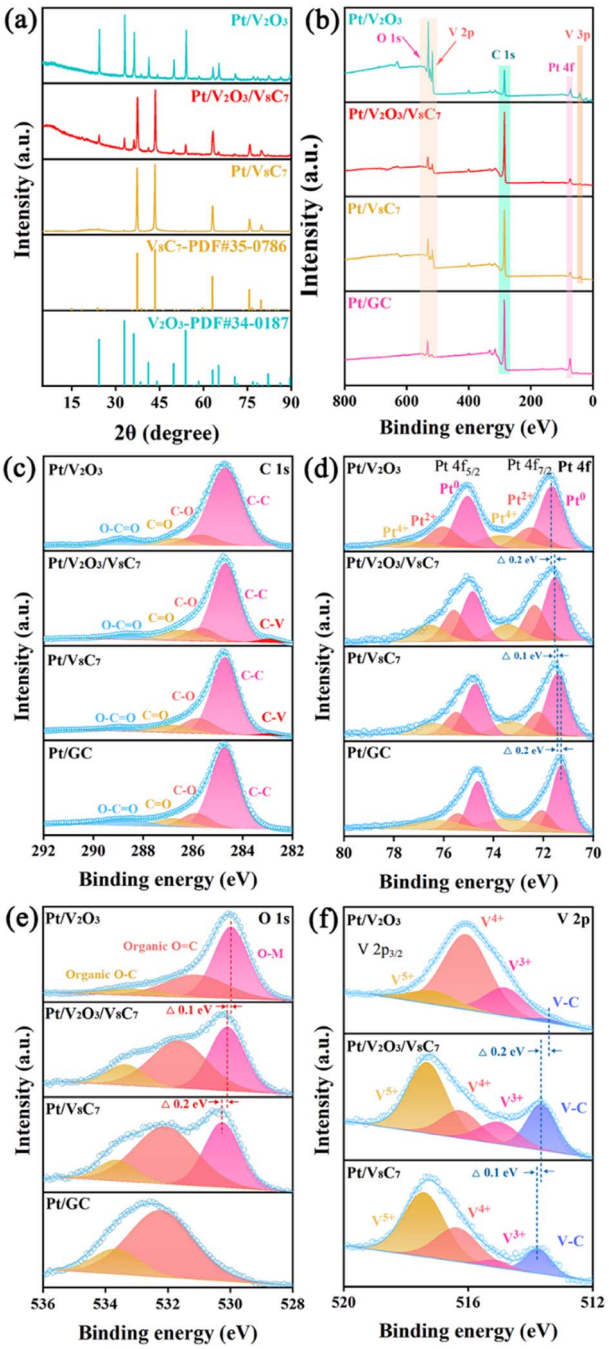

Fig. 2 Crystal structure and surface chemistry of the catalysts. (a) XRD patterns, (b) XPS survey spectra and high-resolution XPS spectra over (c) C 1s, (d) Pt 4f, (e) O 1s, and (f) V 2p regions of the Pt-loaded catalysts.

during synthesis increases. Indeed, the deconvolution of the high-resolution C 1s spectra in Fig. 2c indicates C–C species at the binding energy of 284.8 eV to be dominant in all the samples.[54,55,67] The peaks at higher binding energies of 285.6, 286.7, and 288.8 eV belong to C–O, C=O, and O–C=O species, respectively, which originate from incomplete graphitization of glucose pyrolysis products and are commonly observed with porous carbon materials.[56] For the Pt/V_8C_7 and $Pt/V_2O_3/V_8C_7$ catalysts, another peak at 282.9 eV exists, reflecting the presence

of metal carbide species consistent with the identification of V_8C_7 by XRD.[55,67]

More important information about the electronic structure of the catalysts is revealed by the high-resolution Pt 4f, O 1s, and V 2p spectra in Fig. 2d–f. After deconvolution, the Pt 4f spectra in Fig. 2d indicate the presence of three different Pt species. In $Pt/V_2O_3/V_8C_7$ for example, the signals of metallic Pt^0 are found at 71.5 eV and 74.8 eV, oxidized Pt^{2+} at 72.4 eV and 75.6 eV, and Pt^{4+} at 73.5 eV and 76.6 eV.[11,68] In comparison, the binding energy of the Pt^0 species in Pt/V_2O_3 and Pt/V_8C_7 shifts to higher and lower values, respectively, suggesting that the electron density on Pt^0 follows the order of $Pt/V_8C_7 > Pt/V_2O_3/V_8C_7 > Pt/V_2O_3$. The V 2p spectra exhibit the coexistence of four oxidation states, namely V^{5+}, V^{4+}, V^{3+}, and V carbide (V–C) species.[12,55,69] Taking $Pt/V_2O_3/V_8C_7$ as an example, the four V species appear as peaks at the binding energy of 517.3, 516.2, 515.0, and 513.7 eV, respectively. The V–C species corresponds to the V_8C_7 phase while the V^{5+}, V^{4+}, and V^{3+} can be assigned to V oxides. The presence of V^{5+} and V^{4+} can therefore be attributed to the oxidation of V_2O_3 and/or V_8C_7. The detection of V–C species in Pt/V_2O_3 suggests that some V carbide exists in the form of amorphous or ultrafine crystalline phases that do not manifest themselves in the XRD results. The amount of such phases is minute in Pt/V_2O_3, so the corresponding V–C signal in the C 1s spectrum is overwhelmed by the C–C signal and cannot be reliably resolved. Most importantly, the binding energy of all V 2p peaks (V^{5+}, V^{4+}, V^{3+}, and V–C) shows the opposite trend to that of the Pt 4f peaks, being the highest in Pt/V_8C_7 and lowest in Pt/V_2O_3.

A similar trend is also observed in the O 1s spectra (Fig. 2f), where three types of O in the form of organic O–C, organic O=C, and metal oxide species can be identified at the binding energy of 533.3–533.7, 531.2–532.1, and 530–530.3 eV, respectively.[70–72] The peak associated with metal oxide species shifts toward lower binding energy as the support material changes from V_8C_7 to V_2O_3/V_8C_7 and finally to V_2O_3. Since there are no metal oxide species present in Pt/GC, only those peaks corresponding to organic oxides are observed. The XPS results confirm that V_2O_3 is a better electron acceptor than V_8C_7, leading to more electron transfer from Pt to the support material. Apparently, the extent of such electron transfer depends on the relative amount of V_2O_3 and V_8C_7 as $Pt/V_2O_3/V_8C_7$ exhibits an average effect of the two support phases. It should be noted that compared with GC, V_8C_7 still exhibits an electron-withdrawing effect on Pt, which is evidenced by the Pt 4f binding energy of the catalysts (Fig. 2d). As additional evidence for the electron transfer, the XPS spectra of the V_2O_3, V_8C_7, and V_2O_3/V_8C_7 support materials are presented in Fig. S6.† V oxide, V carbide, and organic C/O species similar to those in the Pt-loaded catalysts are detected. However, in the absence of Pt, the O 1s peak of the metal oxide species and the V 2p peak of the carbide species show no difference in binding energy between the three support materials. The positions of V^{5+} and V^{4+} peaks exhibit a trend that is even opposite to the one observed with the Pt-loaded catalysts, highlighting the presence of strong metal–support interaction.

2.2 DER/HER performance

In 1 M NaOD solution, the DER performance of each catalyst was thoroughly analyzed, as summarized in Fig. 3. The polarization curves in Fig. 3a show that the apparent activity follows the order of $Pt/V_2O_3/V_8C_7$ > 20% Pt/C > Pt/V_8C_7 > Pt/GC > Pt/V_2O_3. $Pt/V_2O_3/V_8C_7$ exhibits outstanding performance, reaching

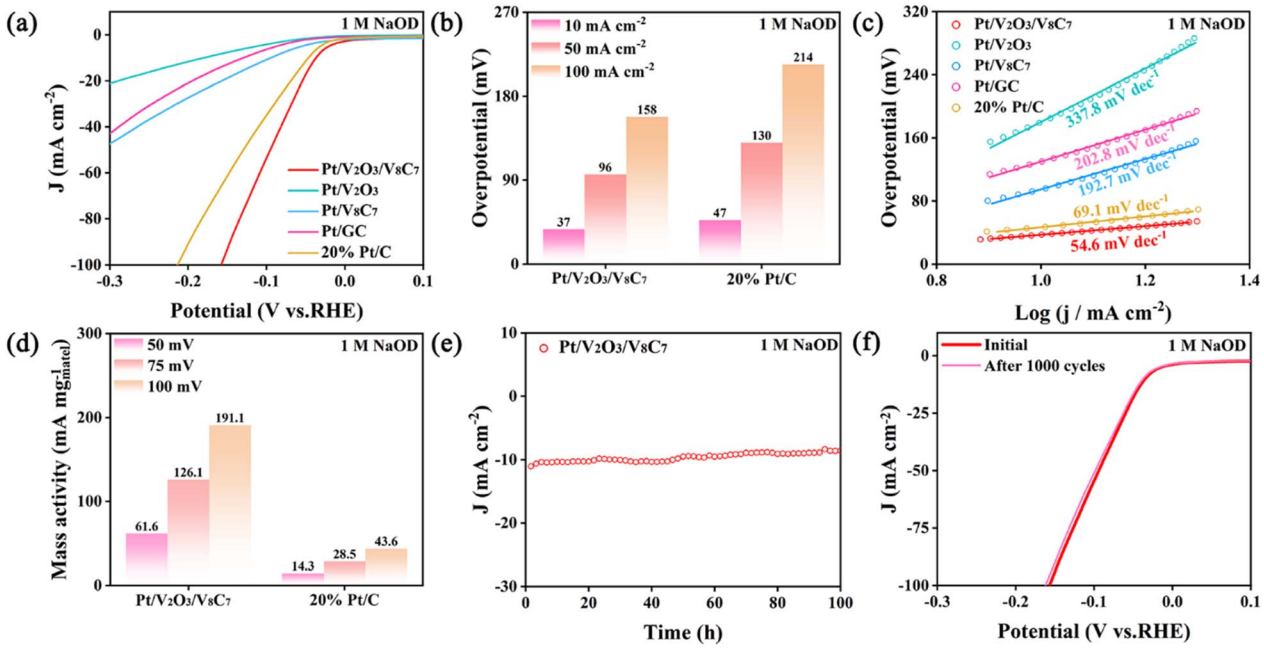

Fig. 3 DER performance in 1 M NaOD. (a) LSV curves (5 mV s^{-1}, 85% *iR* compensation), (b) overpotential at different current densities, (c) Tafel plots, and (d) mass activity based on the amount of Pt. (e) Long-term durability test and (f) accelerated durability test on $Pt/V_2O_3/V_8C_7$.

a current density of 10 mA cm^{-2} with an overpotential of 37 mV, outperforming the commercial 20% Pt/C (47 mV at 10 mA cm^{-2}). The advantage over the commercial benchmark extends to higher current densities, as seen in Fig. 3b. In 1 M KOH and 1 M NaOH, the HER performance of the catalysts shows the same trend, with $Pt/V_2O_3/V_8C_7$ demonstrating superior activity compared to other catalysts (Fig. S7 and S8†). Remarkably, its overpotential at a current density of 10 mA cm^{-2} is only 16 mV in 1 M KOH and 15 mV in 1 M NaOH (see Table S1† for the overpotential of the other catalysts).

As a descriptor of electrochemical kinetics, the Tafel slopes of the catalysts during the DER are compared in Fig. 3c. The values follow the same trend as that of the overpotential, *i.e.*, the catalyst with a lower DER overpotential (at 10 mA cm^{-2}) also exhibits a lower Tafel slope. The data acquired in alkaline HER lead to similar observations (Fig. S7c and S8c†), except that the Tafel slopes are generally lower in the HER. The drastic difference in the Tafel slope between the catalysts is an indicator of possibly different reaction kinetics, which will be discussed in more detail in Section 2.4.

High cost has been a major limitation of Pt-based catalysts, and reducing the Pt content while maintaining catalytic activity is a crucial step in the catalyst development. To gauge the cost-effectiveness of $Pt/V_2O_3/V_8C_7$, its efficiency of precious metal utilization is compared against the commercial Pt/C by normalizing their activity on the basis of Pt mass in the catalysts. As presented in Fig. 3d, S7d and S8d,† the mass activity of $Pt/V_2O_3/V_8C_7$ in alkaline DER/HER is higher than that of commercial Pt/C by up to 4.4 times at the same overpotential, which translates into a possible cost saving on precious metal by 77%.[18] The practical potential of $Pt/V_2O_3/V_8C_7$ is further demonstrated by its stability. During 100 h of potentiostatic electrolysis, the change in current density as seen in Fig. 3e is minimal. The XRD pattern of the spent $Pt/V_2O_3/V_8C_7$ (Fig. S9†) still shows clear diffraction peaks matching with the standard cards of V_2O_3 and V_8C_7, further confirming the structural stability of the catalyst. To simulate the voltage fluctuation of actual electrolyzers, the catalyst was evaluated by the accelerated durability test (ADT). The polarization curves in Fig. 3f differ insignificantly before and after the 1000 cycles of potential swing, signifying the excellent durability of $Pt/V_2O_3/V_8C_7$ under dynamic operating conditions. Consistent results were obtained in HER experiments (Fig. S7e, f and S8e, f†).

In PEM electrolysis of D_2O and H_2O, the catalysts are exposed to low pH which is necessary for high conductivity of the membrane. The harsh electrochemical environment causes severe corrosion problems and rules out the use of most non-noble metal catalysts, making PEM electrolysis the most likely application of the $Pt/V_2O_3/V_8C_7$ catalyst. Therefore, its DER and HER performance under acidic conditions was also evaluated. The results presented in Fig. 4, S10, and Table S2† indicate the DER/HER overpotential and Tafel slope to still follow the order of $Pt/V_2O_3/V_8C_7$ < 20% Pt/C < Pt/V_8C_7 < Pt/GC < Pt/V_2O_3, and $Pt/V_2O_3/V_8C_7$ retains its stability in the strongly acidic 0.5 M D_2SO_4 and 0.5 M H_2SO_4. The HER activity of $Pt/V_2O_3/V_8C_7$ compares closely to that of the best Pt-based catalysts reported recently (Tables S3 and S4†). We highlight its mass activity in 0.5 M D_2SO_4 which is up to 2 times higher than that in 1 M NaOD and 5–9 times higher than that of commercial Pt/C in 0.5 M D_2SO_4 (Fig. 3d and 4d), suggesting $Pt/V_2O_3/V_8C_7$ to be most suitable for application in PEM electrolysis of D_2O.

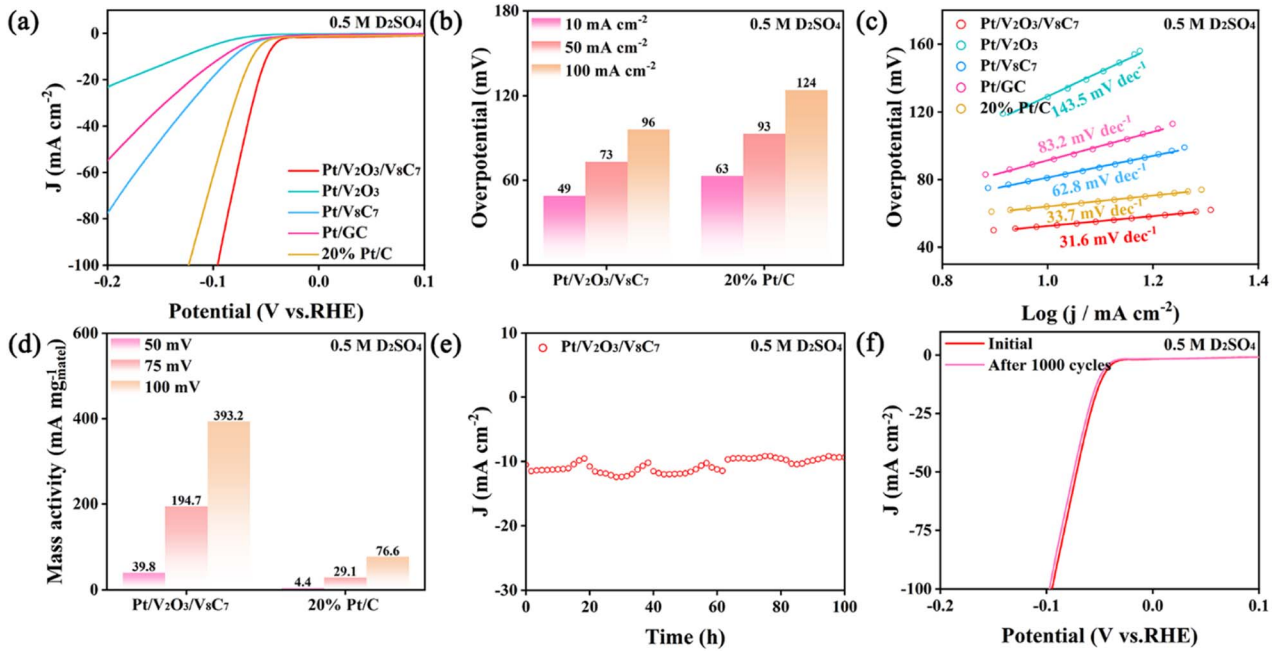

Fig. 4 DER performance in 0.5 M D_2SO_4. (a) LSV curves (5 mV s^{-1}, 85% *iR* compensation), (b) overpotential at different current densities, (c) Tafel plots, and (d) mass activity based on the amount of Pt. (e) Long-term durability test and (f) accelerated durability test on $Pt/V_2O_3/V_8C_7$.

2.3 Application in PEM electrolysis

The realistic performance of $Pt/V_2O_3/V_8C_7$ and commercial Pt/C in PEM electrolysis of D_2O and H_2O was evaluated in an in-house cell with an active electrode area of 1.4 × 1.4 cm^2 on both the anode and cathode. The structure of the device is illustrated in Fig. 5a (The photograph of the PEM set-up is shown in Fig. S11†). $Pt/V_2O_3/V_8C_7$ or commercial Pt/C serves as the cathode catalyst and commercial IrO_2 nanoparticles the anode catalyst. As evident from Fig. 5b, in the wide range of current densities tested, the cell voltage for D_2O electrolysis is remarkably lower when $Pt/V_2O_3/V_8C_7$ is used. At 1000 mA cm^{-2} for example, the difference amounts to 0.5 V which equals 20% reduction in the energy requirement of the cell. The H_2O electrolysis performance of $Pt/V_2O_3/V_8C_7$ is also superior to that of commercial Pt/C, with a difference of 0.43 V in cell voltage at 1000 mA cm^{-2} (Fig. S12a†). During 25 h of continuous operation at 1000 mA cm^{-2}, the performance of the PEM cell adopting the $Pt/V_2O_3/V_8C_7$ catalyst displays negligible decay in either D_2O or H_2O electrolysis (Fig. 5c and S12b†). Moreover, the faradaic efficiency of D_2 production during the sustained electrolysis is close to 100% (Fig. 5d), confirming minimal contribution of side reactions. These findings underscore the promising application of $Pt/V_2O_3/V_8C_7$ in practical PEM set-ups.

2.4 Mechanism of activity enhancement

The DER/HER performance above has evidenced the synergistic effects of V_2O_3 and V_8C_7 on tuning the activity of supported Pt nanoclusters. Such effects can be linked to the electron transfer detected by XPS apparently, but more in-depth analysis of the mechanism behind is necessary to the understanding and generalization of the strategy for catalyst development. Given the scarcity of DER research in open literature, we focus on the HER behavior which has a more established basis of mechanistic studies. The apparent activity presented so far is normalized either by the projected geometric area of the electrode or by the mass of Pt, making itself a manifestation of the combined effects of intrinsic activity and amount of accessible catalytic surface. Accurate mechanistic analysis requires isolation of each factor, which is realized by determining the electrochemically active surface area (ECSA).

Underpotential deposition (UPD) and stripping of Cu is a surface-sensitive characterization technique that is widely used to measure the ECSA. The cyclic voltammogram in Fig. 6a shows clear features of UPD and stripping of Cu in $Pt/V_2O_3/V_8C_7$. Similar features are observed for other catalysts in Fig. S13.† The amount of charge transfer associated with the stripping process was used to calculate the ECSA by assuming a conversion factor of 420 μC cm^{-2} of active surface.[73] The results plotted in Fig. 6b show that the high apparent activity of $Pt/V_2O_3/V_8C_7$ and especially commercial Pt/C can be attributed in part to their large ECSA. On the other hand, the low ECSA of Pt/GC accounts for its poor performance compared with commercial Pt/C to some extent. This confirms the low Pt dispersion found by TEM (Fig. S3†). We proceed to normalize the HER current in 0.5 M H_2SO_4 by the ECSA, and the resulting polarization curves, reflecting the intrinsic activity of each catalyst, are presented in Fig. 6c. In terms of intrinsic activity, $Pt/V_2O_3/V_8C_7$ still outperforms other catalysts obviously while Pt/V_2O_3 is the worst. The difference has to be explained by the different kinetics specific to each catalyst.

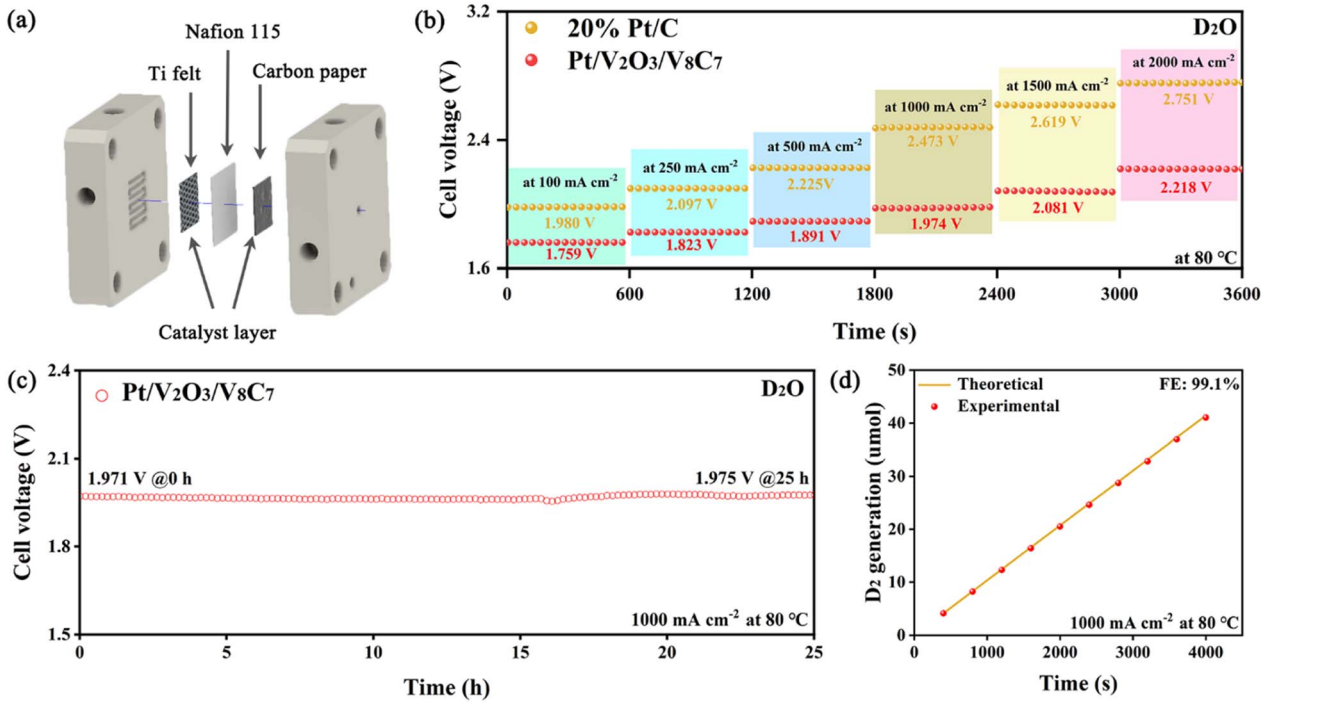

Fig. 5 PEM electrolysis of D_2O. (a) Schematic illustration of the PEM device. (b) Cell voltage at different current densities. (c) Stability test and (d) faradaic efficiency of D_2 production with $Pt/V_2O_3/V_8C_7$.

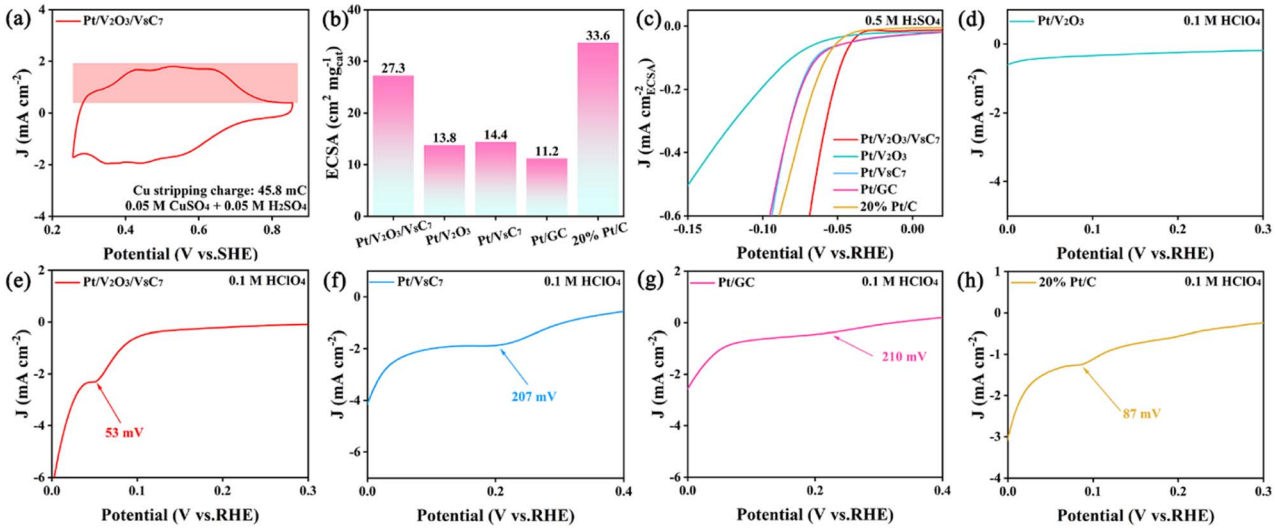

Fig. 6 Electrochemical mechanistic study on the catalysts. (a) Underpotential deposition-stripping of Cu on $Pt/V_2O_3/V_8C_7$. (b) ECSA derived from Cu stripping charge, (c) ECSA-normalized LSV curves in 0.5 M H_2SO_4, and (d–h) underpotential deposition of H in 0.1 M $HClO_4$ for the Pt-loaded catalysts.

Generally, the HER in an acidic environment can be described by the following elementary reactions where * denotes an active site and H* an adsorbed H atom (eqn (1)–(3)).[74,75]

$$H^+ + * + e^- \rightarrow H^* \text{ (Volmer reaction);} \quad (1)$$

$$H^* + H^+ + e^- \rightarrow H_2 + * \text{ (Heyrovsky reaction);} \quad (2)$$

$$2H^* \rightarrow H_2 + 2^* \text{ (Tafel reaction)} \quad (3)$$

It is easily seen that the properties of the only adsorbed intermediate species, H*, govern the reaction mechanism. A high kinetic barrier to its formation leads to a HER rate controlled by Step 1, while the rate determining step (RDS) becomes Step 2 or 3 if desorption of H is more difficult. In the ideal case where the kinetic barrier to both adsorption and desorption of H is low such that its thermal energy is sufficient to drive its desorption, Step 3 is the RDS. By assuming the activation energy to scale linearly with the reaction energy of H adsorption, the latter also known as the hydrogen binding energy (HBE) becomes a convenient descriptor of HER kinetics that has proven successful in explaining the activity of pure metals.[76,77] Thus, Step 1 is expected to be the RDS for positive HBE, Step 2 the RDS for significantly negative HBE, and ideally the kinetics is limited by Step 3 for HBE $\approx$ 0.

The HBE can be experimentally measured by the potential at which UPD of H occurs ($E_{UPD,\ H}$) through the approximation HBE $\approx -eE_{UPD,\ H}$.[78] The polarization curves in Fig. 6d–h display clear features of H UPD for all the catalysts except Pt/V_2O_3 ($HClO_4$ was chosen as the electrolyte to minimize the interference of adsorbed anions). The positions of the UPD features indicate Pt/GC to have the most negative HBE, followed closely by Pt/V_8C_7. The HBE of commercial Pt/C and $Pt/V_2O_3/V_8C_7$ is mildly negative with the latter closest to 0. The trend matches that of the XPS binding energy shift of the Pt, V, and O species in the catalysts, suggesting that electron transfer from Pt to the support weakens H adsorption. The absence of H UPD for Pt/V_2O_3 is therefore interpreted as a positive HBE due to excessive electron transfer to the support. According to the measured HBE, an adsorption-limited HER kinetics is expected for Pt/V_2O_3 while the other catalysts should exhibit desorption-limited kinetics. The high intrinsic activity of $Pt/V_2O_3/V_8C_7$ is thus explained by its smallest negative HBE that renders H adsorption thermodynamically favored while minimizing the energy barrier to H desorption. Pt/V_2O_3, on the other hand, has poor intrinsic activity caused by the difficulty in forming H*. From the perspective of catalyst design, the results above mean that the metal–support interaction is too strong for Pt/V_2O_3 to optimize H adsorption, while it is too weak for Pt/V_8C_7 as reflected by the similar HBE of Pt/V_8C_7 and Pt/GC. Improvement over the benchmark Pt/C is only possible with the V_2O_3/V_8C_7 composite support, which appears to be able to balance the electronic effect of the individual components.

Besides HBE, Tafel analysis is another powerful tool to probe the reaction kinetics. In the HER, the Tafel slopes of 120, 40, and 30 mV dec^{-1} have been commonly cited for the RDSs being Steps 1, 2, and 3, respectively.[79,80] As can be seen in Fig. S10c,† the Tafel slope of $Pt/V_2O_3/V_8C_7$, commercial Pt/C, Pt/V_8C_7, Pt GC, and Pt/V_2O_3 is 30, 32, 43, 56, and 127 mV dec^{-1}, respectively. The values indicate the HER kinetics on $Pt/V_2O_3/V_8C_7$ and commercial Pt/C to be limited by Step 3, Pt/V_8C_7 and Pt/GC by Step 2, and Pt/V_2O_3 by Step 1, which is consistent with the prediction by their HBE. Similar Tafel slopes measured in D_2SO_4 (Fig. 4c) suggest that the discussion above also applies to the DER. This further corroborates the mechanism of performance enhancement induced by the electronic metal–support interaction.

3. Conclusions

In this study, a finely dispersed $Pt/V_2O_3/V_8C_7$ catalyst was successfully synthesized by controlled carbonization of the support material followed by wet impregnation. The metal–support interaction between Pt, V_2O_3 and V_8C_7 was systematically investigated in the context of the DER and HER. The $Pt/V_2O_3/V_8C_7$ catalyst exhibited superior catalytic activity and excellent stability in the DER/HER, outperforming commercial Pt/C and realizing up to 20% reduction in cell voltage during D_2O/H_2O electrolysis in a practical PEM device at industrially relevant current densities. TEM, XRD, and Cu UPD/stripping results revealed high metal dispersion and ECSA of $Pt/V_2O_3/V_8C_7$. XPS, H UPD, and Tafel slope measurements indicated electron transfer from Pt to V_2O_3 and/or V_8C_7 which shifted the HBE toward positive values and changed DER/HER pathways. Both factors described are crucial to the high DER/HER activity of $Pt/V_2O_3/V_8C_7$. However, the electronic effect of V_2O_3 alone is too strong on Pt while that of V_8C_7 is too weak to facilitate the optimization of HBE. Near-zero HBE that is ideal for fast DER/HER kinetics was only achieved by the V_2O_3/V_8C_7 dual support system with balanced effects. It is reasonable to expect that the strategy of performance enhancement by multi-component catalyst supports applies to other metals as well. This study not only provides insights into electronic metal–support interactions in structurally complex catalysts but also highlights the broad industrial prospects of utilizing such effects in the development of practical electrocatalysts.

Conflicts of interest

There are no conflicts to declare.

Acknowledgements

The authors acknowledge the financial support from the National Key R & D Program of China (2021YFA1500900), and the National Natural Science Foundation of China (22308326, 22141001).

Notes and references

1 C. Hu, L. Zhang and J. Gong, *Energy Environ. Sci.*, 2019, **12**, 2620–2645.
2 S. Ji, Y. Chen, S. Zhao, W. Chen, L. Shi, Y. Wang, J. Dong, Z. Li, F. Li, C. Chen, Q. Peng, J. Li, D. Wang and Y. Li, *Angew. Chem., Int. Ed.*, 2019, **58**, 4271–4275.
3 B. Zhang, C. Qiu, S. Wang, H. Gao, K. Yu, Z. Zhang, X. Ling, W. Ou and C. Su, *Sci. Bull.*, 2021, **66**, 562–569.
4 J. Anglister, *Q. Rev. Biophys.*, 1990, **23**, 175–203.
5 S. Kopf, F. Bourriquen, W. Li, H. Neumann, K. Junge and M. Beller, *Chem. Rev.*, 2022, **122**, 6634–6718.
6 N. Li, Y. Li, X. Wu, C. Zhu and J. Xie, *Chem. Soc. Rev.*, 2022, **51**, 6291–6306.
7 Y. Li, G. Wang, Z. Bao, F. Shao, X. Peng, Y. Shao, S. Zhang and J. Wang, *Chem. Eng. J.*, 2023, **471**, 144491.
8 G. Prakash, N. Paul, G. A. Oliver, D. B. Werz and D. Maiti, *Chem. Soc. Rev.*, 2022, **51**, 3123–3163.
9 T. Driesner, *Science*, 1997, **277**, 791–794.
10 A. Enomoto, S. Kajita and K.-i. Fujita, *Chem. Lett.*, 2018, **48**, 106–109.
11 Y. Li, S. Zhang, W. Xu, C. Jiang, L. Shao, S. Wang and J. Wang, *J. Mater. Chem. A*, 2023, **11**, 4000–4006.
12 Y. Li, W. Xu, Y. Sheng, C. Jiang, N. Wang, Y. Chen, Z. Ma, L. Shao, S. Wang, S. Zhang and J. Wang, *AIChE J.*, 2023, DOI: **10.1002/aic.18310**.
13 Q. Hu, K. Gao, X. Wang, H. Zheng, J. Cao, L. Mi, Q. Huo, H. Yang, J. Liu and C. He, *Nat. Commun.*, 2022, **13**, 3958.
14 Q. Hu, S. Qi, Q. Huo, Y. Zhao, J. Sun, X. Chen, M. Lv, W. Zhou, C. Feng, X. Chai, H. Yang and C. He, *J. Am. Chem. Soc.*, 2024, **146**, 2967–2976.
15 X. Li, C. Deng, Y. Kong, Q. Huo, L. Mi, J. Sun, J. Cao, J. Shao, X. Chen, W. Zhou, M. Lv, X. Chai, H. Yang, Q. Hu and C. He, *Angew. Chem., Int. Ed.*, 2023, **62**, e202309732.
16 X. Li, H. Zhang, Q. Hu, W. Zhou, J. Shao, X. Jiang, C. Feng, H. Yang and C. He, *Angew. Chem., Int. Ed.*, 2023, **62**, e202300478.
17 R. Abbasi, B. P. Setzler, S. Lin, J. Wang, Y. Zhao, H. Xu, B. Pivovar, B. Tian, X. Chen, G. Wu and Y. Yan, *Adv. Mater.*, 2019, **31**, 1805876.
18 Q. Cheng, C. Hu, G. Wang, Z. Zou, H. Yang and L. Dai, *J. Am. Chem. Soc.*, 2020, **142**, 5594–5601.
19 H. Jin, B. Ruqia, Y. Park, H. J. Kim, H.-S. Oh, S.-I. Choi and K. Lee, *Adv. Energy Mater.*, 2021, **11**, 2003188.
20 Z. Kang, G. Yang, J. Mo, Y. Li, S. Yu, D. A. Cullen, S. T. Retterer, T. J. Toops, G. Bender, B. S. Pivovar, J. B. Green and F.-Y. Zhang, *Nano Energy*, 2018, **47**, 434–441.
21 R. Ogawa, R. Tanii, R. Dawson, H. Matsushima and M. Ueda, *Energy*, 2018, **149**, 98–104.
22 S. Shibuya, H. Matsushima and M. Ueda, *J. Electrochem. Soc.*, 2016, **163**, F704.
23 J. Xu, R. Li, X. Yan, Q. Zhao, R. Zeng, J. Ba, Q. Pan, X. Xiang and D. Meng, *Nano Res.*, 2022, **15**, 3952–3958.
24 N. Zeng, C. Hu, C. Lv, A. Liu, L. Hu, Y. An, P. Li, M. Chen, X. Zhang, M. Wen, K. Chen, Y. Yao, J. Cai and T. Tang, *Sep. Purif. Technol.*, 2023, **310**, 123148.
25 J. Zheng, X. Sun, J. Hu, S. Wang, Z. Yao, S. Deng, X. Pan, Z. Pan and J. Wang, *ACS Appl. Mater. Interfaces*, 2021, **13**, 50878–50891.
26 S. Wang, G. Feng, W. Xu, W. Li and J. Wang, *Comput. Mater. Sci.*, 2023, **229**, 112397.
27 A. D. Buckingham and L. Fan-Chen, *Int. Rev. Phys. Chem.*, 1981, **1**, 253–269.
28 R. Mills and K. R. Harris, *Chem. Soc. Rev.*, 1976, **5**, 215–231.
29 L. G. van der Wel, V. Gkinis, V. A. Pohjola and H. A. J. Meijer, *J. Glaciol.*, 2011, **57**, 30–38.
30 T. Green and D. Britz, *J. Electroanal. Chem.*, 1996, **412**, 59–66.
31 A. Hodges, A. L. Hoang, G. Tsekouras, K. Wagner, C.-Y. Lee, G. F. Swiegers and G. G. Wallace, *Nat. Commun.*, 2022, **13**, 1304.
32 J. N. Tiwari, S. Sultan, C. W. Myung, T. Yoon, N. Li, M. Ha, A. M. Harzandi, H. J. Park, D. Y. Kim, S. S. Chandrasekaran, W. G. Lee, V. Vij, H. Kang, T. J. Shin,

H. S. Shin, G. Lee, Z. Lee and K. S. Kim, *Nat. Energy*, 2018, **3**, 773–782.
33 Z. Zeng, S. Küspert, S. E. Balaghi, H. E. M. Hussein, N. Ortlieb, M. Knäbbeler-Buß, P. Hügenell, S. Pollitt, N. Hug, J. Melke and A. Fischer, *Small*, 2023, **19**(29), 2205885.
34 M. Li, C. Qiu, T. Sun, X. Wang, L. Xia, X. Yang, W. Zhao, H. Shi, L. Ding, X. Zhong, Y. Zhu and J. Wang, *Ind. Eng. Chem. Res.*, 2023, **62**, 7889–7900.
35 S. Li, W. Xie, Y. Song, Y. Li, Y. Song, J. Li and M. Shao, *Chem. Eng. J.*, 2022, **437**, 135473.
36 S. Wang, B. Xu, W. Huo, H. Feng, X. Zhou, F. Fang, Z. Xie, J. K. Shang and J. Jiang, *Appl. Catal., B*, 2022, **313**, 121472.
37 K. Deng, T. Zhou, Q. Mao, S. Wang, Z. Wang, Y. Xu, X. Li, H. Wang and L. Wang, *Adv. Mater.*, 2022, **34**, 2110680.
38 F. Podjaski, D. Weber, S. Zhang, L. Diehl, R. Eger, V. Duppel, E. Alarcón-Lladó, G. Richter, F. Haase, A. Fontcuberta i Morral, C. Scheu and B. V. Lotsch, *Nat. Catal.*, 2020, **3**, 55–63.
39 J. Zhang, G. Wang, Z. Liao, P. Zhang, F. Wang, X. Zhuang, E. Zschech and X. Feng, *Nano Energy*, 2017, **40**, 27–33.
40 H. Gao, Y. Jiang, R. Chen, C.-L. Dong, Y.-C. Huang, M. Ma, Z. Shi, J. Liu, Z. Zhang, M. Qiu, T. Wu, J. Wang, Y. Jiang, J. Chen, X. An, Y. He and S. Wang, *Adv. Funct. Mater.*, 2023, **33**, 2214795.
41 P. Wu, S. Tan, J. Moon, Z. Yan, V. Fung, N. Li, S.-Z. Yang, Y. Cheng, C. W. Abney, Z. Wu, A. Savara, A. M. Momen, D.-e. Jiang, D. Su, H. Li, W. Zhu, S. Dai and H. Zhu, *Nat. Commun.*, 2020, **11**, 3042.
42 S. Shanmugapriya, P. Zhu, M. Ganeshbabu, Y. Sung Lee, X. Zhang and R. Kalai Selvan, *Mater. Sci. Eng., B*, 2022, **284**, 115880.
43 H. Sun, C.-W. Tung, Y. Qiu, W. Zhang, Q. Wang, Z. Li, J. Tang, H.-C. Chen, C. Wang and H. M. Chen, *J. Am. Chem. Soc.*, 2022, **144**, 1174–1186.
44 X. Zheng, L. Li, M. Deng, J. Li, W. Ding, Y. Nie and Z. Wei, *Catal. Sci. Technol.*, 2020, **10**, 4743–4751.
45 Y.-Y. Hung, W.-S. Liu, Y.-C. Chen, K.-W. Wang and T.-P. Perng, *Int. J. Hydrogen Energy*, 2020, **45**, 14083–14092.
46 Y. Yang, D. Wu, R. Li, P. Rao, J. Li, P. Deng, J. Luo, W. Huang, Q. Chen, Z. Kang, Y. Shen and X. Tian, *Appl. Catal., B*, 2022, **317**, 121796.
47 T. Ma, H. Cao, S. Li, S. Cao, Z. Zhao, Z. Wu, R. Yan, C. Yang, Y. Wang, P. A. van Aken, L. Qiu, Y.-G. Wang and C. Cheng, *Adv. Mater.*, 2022, **34**(41), 2206368.
48 N. S. Powar, C. B. Hiragond, D. Bae and S.-I. In, *J. CO_2 Util.*, 2022, **55**, 101814.
49 J. Li, J. Wang, Y. Liu, C. Yuan, G. Liu, N. Wu and X. Liu, *Catal. Sci. Technol.*, 2022, **12**, 4498–4510.
50 H. Jun, S. Kim and J. Lee, *Korean J. Chem. Eng.*, 2020, **37**, 1317–1330.
51 S. Park, Y.-L. Lee, Y. Yoon, S. Y. Park, S. Yim, W. Song, S. Myung, K.-S. Lee, H. Chang, S. S. Lee and K.-S. An, *Appl. Catal., B*, 2022, **304**, 120989.
52 Y. Yoon, A. P. Tiwari, M. Choi, T. G. Novak, W. Song, H. Chang, T. Zyung, S. S. Lee, S. Jeon and K.-S. An, *Adv. Funct. Mater.*, 2019, **29**, 1903443.
53 X. Peng, L. Hu, L. Wang, X. Zhang, J. Fu, K. Huo, L. Y. S. Lee, K.-Y. Wong and P. K. Chu, *Nano Energy*, 2016, **26**, 603–609.
54 A. Pajares, H. Prats, A. Romero, F. Viñes, P. R. de la Piscina, R. Sayós, N. Homs and F. Illas, *Appl. Catal., B*, 2020, **267**, 118719.
55 M. Shao, H. Chen, S. Hao, H. Liu, Y. Cao, Y. Zhao, J. Jin, H. Dang, Y. Meng, Y. Huo and L. Cui, *Appl. Surf. Sci.*, 2022, **577**, 151857.
56 X. Fan, C. Liu, B. Gao, H. Li, Y. Zhang, H. Zhang, Q. Gao, X. Cao and Y. Tang, *Small*, 2023, **19**, 2301178.
57 Y. Li, S. Wang, Y. Hu, X. Zhou, M. Zhang, X. Jia, Y. Yang, B.-L. Lin and G. Chen, *J. Mater. Chem. A*, 2022, **10**, 5273–5279.
58 J. Yu, X. Gao, G. Chen and X. Yuan, *Int. J. Hydrogen Energy*, 2016, **41**, 4150–4158.
59 Y. Duan, X.-L. Zhang, F.-Y. Gao, Y. Kong, Y. Duan, X.-T. Yang, X.-X. Yu, Y.-R. Wang, S. Qin, Z. Chen, R. Wu, P.-P. Yang, X.-S. Zheng, J.-F. Zhu, M.-R. Gao, T.-B. Lu, Z.-Y. Yu and S.-H. Yu, *Angew. Chem., Int. Ed.*, 2023, **62**, e202217275.
60 S. Chalotra, R. A. Mir, G. Kaur and O. P. Pandey, *Ceram. Int.*, 2020, **46**, 703–714.
61 H. Xu, L. Liu, J. Gao, P. Du, G. Fang and H.-J. Qiu, *ACS Appl. Mater. Interfaces*, 2019, **11**, 38746–38753.
62 P. Wu, J. Li, Z. Xiao, Y. Zhao, Y. Wang, B. Xiao and B. Huang, *Chem. Commun.*, 2021, **57**, 10395–10398.
63 J. Liu, Y. Zhou, J. Wang, Y. Pan and D. Xue, *Chem. Commun.*, 2011, **47**, 10380–10382.
64 X.-Z. Fan, Q.-Q. Pang, F. Fan, H.-C. Yao and Z.-J. Li, *Int. J. Hydrogen Energy*, 2023, **48**(54), 20577–20587.
65 L. Zhang, Y. Liu, Z. Zhao, P. Jiang, T. Zhang, M. Li, S. Pan, T. Tang, T. Wu, P. Liu, Y. Hou and H. Lu, *ACS Nano*, 2020, **14**, 8495–8507.
66 F. Wang, Q. Zhang, Z. Rui, J. Li and J. Liu, *ACS Appl. Mater. Interfaces*, 2020, **12**, 30381–30389.
67 J. Wu, J. Zhao, B. Vaidhyanathan, H. Zhang, A. Anshuman, A. Nare and S. Saremi-Yarahmadi, *Materialia*, 2020, **13**, 100833.
68 Z. Li, W. Niu, Z. Yang, N. Zaman, W. Samarakoon, M. Wang, A. Kara, M. Lucero, M. V. Vyas, H. Cao, H. Zhou, G. E. Sterbinsky, Z. Feng, Y. Du and Y. Yang, *Energy Environ. Sci.*, 2020, **13**, 884–895.
69 F. N. I. Sari, H.-S. Chen, A. k. Anbalagan, Y.-J. Huang, S.-C. Haw, J.-M. Chen, C.-H. Lee, Y.-H. Su and J.-M. Ting, *Chem. Eng. J.*, 2022, **438**, 135515.
70 S. Zhang, H. Zhuo, S. Li, Z. Bao, S. Deng, G. Zhuang, X. Zhong, Z. Wei, Z. Yao and J.-g. Wang, *Catal. Today*, 2021, **368**, 187–195.
71 S. Zhang, G. Feng, Z. Bao, X. Peng, C. Jiang, Y. Shao, S. Wang and J. Wang, *Ind. Eng. Chem. Res.*, 2023, **62**, 6113–6120.
72 C. Jiang, Y.-F. Fei, W. Xu, Z. Bao, Y. Shao, S. Zhang, Z.-T. Hu and J. Wang, *Appl. Catal., B*, 2023, **334**, 122867.
73 M. Shao, J. H. Odell, S.-I. Choi and Y. Xia, *Electrochem. Commun.*, 2013, **31**, 46–48.
74 H.-J. Liu, S. Zhang, Y.-M. Chai and B. Dong, *Angew. Chem., Int. Ed.*, 2023, **62**, e202313845.
75 Y. Jia, T.-H. Huang, S. Lin, L. Guo, Y.-M. Yu, J.-H. Wang, K.-W. Wang and S. Dai, *Nano Lett.*, 2022, **22**, 1391–1397.

76 J. K. Nørskov, T. Bligaard, A. Logadottir, J. R. Kitchin, J. G. Chen, S. Pandelov and U. Stimming, *J. Electrochem. Soc.*, 2005, **152**, J23.
77 M. T. M. Koper, *J. Solid State Electrochem.*, 2013, **17**, 339–344.
78 N. Dubouis and A. Grimaud, *Chem. Sci.*, 2019, **10**, 9165–9181.
79 X. Zhang, Z. Luo, P. Yu, Y. Cai, Y. Du, D. Wu, S. Gao, C. Tan, Z. Li, M. Ren, T. Osipowicz, S. Chen, Z. Jiang, J. Li, Y. Huang, J. Yang, Y. Chen, C. Y. Ang, Y. Zhao, P. Wang, L. Song, X. Wu, Z. Liu, A. Borgna and H. Zhang, *Nat. Catal.*, 2018, **1**, 460–468.
80 Y. Wang, Q. Lu, F. Li, D. Guan and Y. Bu, *Adv. Funct. Mater.*, 2023, **33**, 2213523.